American Mineralogist, Volume 110, pages 933–940, 2025

Thermal expansion of römerite under low-temperature conditions

Eli Bird[1,*], Olivia S. Pardo[1,†], Nina Gilkyson[1,‡], and Jennifer M. Jackson[1,§]

[1]Seismological Laboratory, California Institute of Technology, Pasadena, California 91125, U.S.A.

Abstract

Römerite, a triclinic hydrous sulfate in the $P\bar{1}$ space group with the chemical formula $Fe^{2+}Fe_2^{3+}(SO_4)_4{\cdot}14(H_2O)$, is of potential interest in studies of planetary environments, with particular relevance to Mars and the icy jovian satellites. Past work has indicated the presence of hydrous sulfates on said bodies, and the mixed-valence iron in römerite's structure makes the mineral a worthwhile end-member composition in thermodynamic models. Such models should be constrained by measurements at the low temperatures relevant to the planetary environments in question. We characterized single crystals of römerite with time-domain Mössbauer spectroscopy, Raman spectroscopy, and X-ray diffraction methods. Through our X-ray diffraction experiment, we refined the unit-cell parameters of the crystal between 100 and 300 K. The resulting temperature-variant lattice parameters and volumes are reported and are fit by physical and empirical models of the thermal expansion coefficient. The physical model considered, a Debye model of thermal expansion, provides estimates of additional thermodynamic parameters: the ratio of the bulk modulus at 0 K and 1 bar to the thermodynamic Grüneisen parameter ($K_{0,0K}/\gamma_{th}$), the volume at 0 K and 1 bar ($V_{0,0K}$), and the Debye temperature (θ_D).

Keywords: Römerite, hydrous sulfate, low temperature, X-ray diffraction, icy satellites, thermal expansion, Mössbauer spectroscopy, Raman spectroscopy

Introduction

Römerite is a mixed-valence, iron-bearing hydrous sulfate with the nominal chemical formula $Fe^{2+}Fe_2^{3+}(SO_4)_4{\cdot}14(H_2O)$ (Fig. 1). Its structure is triclinic, with space group $P\bar{1}$. The unit cell of römerite contains two unique sulfate tetrahedra and two unique octahedra, which host iron that is sixfold coordinated with oxygen. The two octahedra contain ferric (Fe^{3+}) and ferrous (Fe^{2+}) iron, respectively (Fanfani et al. 1970). The Fe^{2+}-centered octahedra are fully hydrated [i.e., $Fe^{2+}(H_2O)_6$]. In contrast, the ferric iron cations are bonded to only four water groups, with the remaining two vertices of the octahedra composed of oxygen atoms bridging to the sulfate tetrahedra.

On Earth, römerite is primarily formed through the oxidation of sulfide deposits, but it may have greater relevance to other planetary bodies, such as Mars and the icy satellites of Jupiter, either directly or acting as an end-member composition in broader models of hydrous sulfates (Fanfani et al. 1970; Mauro et al. 2019).

Remote spectroscopic measurements of Mars and of icy satellites have been interpreted as indicating the presence of hydrous sulfates. On Mars, visible and near-infrared spectroscopy has identified hydrous sulfates as constituents of wide-ranging geologic features, including plains, canyon troughs, and impact craters (Bishop et al. 2009; Murchie et al. 2009; Lichtenberg et al. 2010). Dalton et al. (2012) proposed that near-infrared spectra of three bright plains with dark lineae on Europa, all observed by the Galileo spacecraft, are best fit by compositions with significant hydrous sulfate components (9–22%). In addition, lower albedo plains and nearby ridged plains, also observed by the spacecraft, were modeled as having compositions with 62% and 27% hydrated sulfate material, respectively, and römerite could act as a valuable end-member in models of the features, alongside purely ferrous and ferric species (Shirley et al. 2010).

Both Mars and the icy satellites observe surface temperatures far below those on Earth, ranging from 170 to 290 K on Mars and 40 to 120 K on Europa (Martínez et al. 2017; Ashkenazy 2019). Thus, to characterize the interplay of römerite with either system, one must understand its low-temperature behavior, with the temperature-variant atomic structure of its unit cell being a critical first-order constraint on said behavior.

Our study reports new single-crystal X-ray diffraction (XRD) and synchrotron Mössbauer spectroscopy (SMS) data, with XRD measurements performed at low temperatures relevant to the planetary bodies discussed above.

Models of Thermal Expansion

In characterizing the response of a crystal structure to varying temperature, a meaningful thermodynamic parameter is the thermal expansion coefficient:

$$\alpha = \frac{1}{V}\left(\frac{\partial V}{\partial T}\right)_P \tag{1}$$

where α is the volumetric thermal expansion (K^{-1}) at constant pressure (P), V is the unit-cell volume, and T is the temperature. A commonly used empirical fit, discussed in Fei (1995) is:

$$\alpha(T) = a_0 + a_1 T + a_2 T^{-2} \tag{2}$$

where a_0, a_1, and a_2 are empirical constants, and

$$V(T) = V_{T_r}\ \exp\left[\int_{T_r}^{T} \alpha(T)dT\right] \tag{3}$$

* Corresponding author E-mail: elijahjosephbird@gmail.com Orcid https://orcid.org/0000-0002-9428-0650
† Orcid https://orcid.org/0000-0003-3964-9272
‡ Present address: Department of Earth, Environmental, and Planetary Sciences, Brown University, Providence, RI 02912, U.S.A.
§ Orcid https://orcid.org/0000-0002-8256-6336

0003-004X/25/0006–933$05.00/DOI: https://doi.org/10.2138/am-2024-9432

Downloaded from http://pubs.geoscienceworld.org/msa/ammin/article-pdf/110/6/933/7212453/ammin-2024-9432.1.pdf
by California Institute of Technology , Elijah Bird

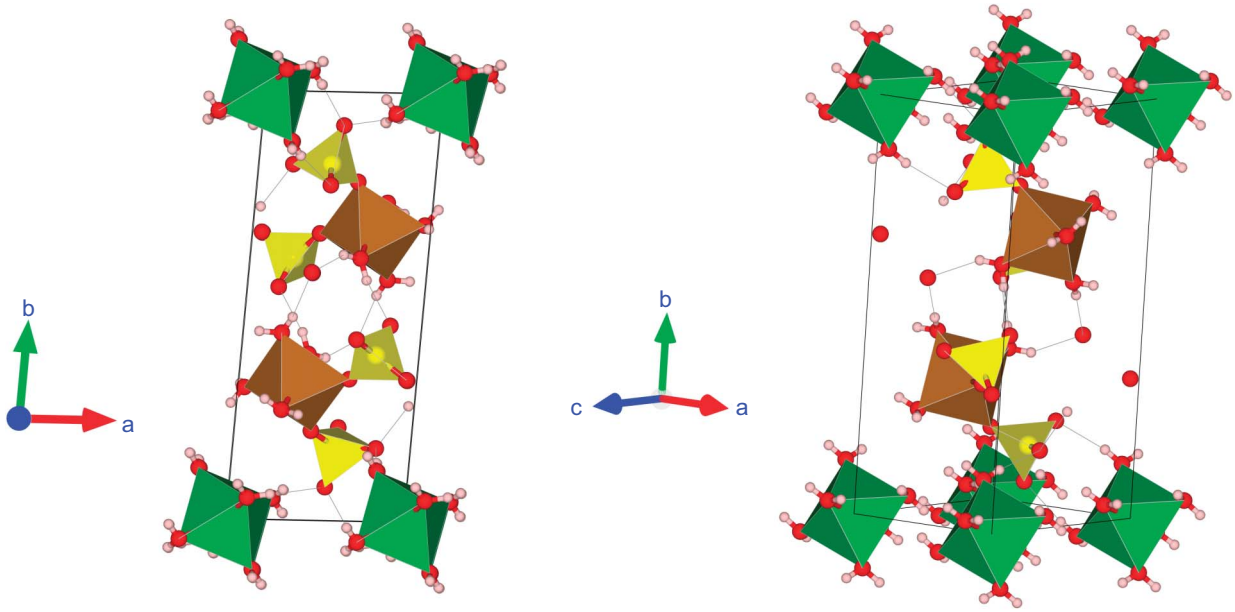

Figure 1. Römerite unit cell at two orientations. Sulfate tetrahedra are plotted in yellow, Fe^{3+}-centered octahedra are plotted in brown, and Fe^{2+}-centered octahedra are plotted in green.

Here, T_r is a reference temperature (in K), and V_{T_r} is the unit-cell volume at said reference temperature (in Å^3).

Physical models of thermal expansion parameterize the energy of lattice vibrations and its relation to thermal expansion. The Debye model is one approximation of the energy of lattice vibrations, which assumes a constant velocity for all vibrational modes, with the vibrational spectrum extending to a maximum frequency ω_D and associated cut-off temperature $\theta_D = \frac{\hbar\omega_D}{k_B}$. Here, ω_D is in Hz, θ_D is in K, $\hbar$ is the reduced Planck constant in J·Hz^{-1}, and k_B is the Boltzmann constant in J·K^{-1}. Such a formulation results in a parabolic-shaped phonon density of states and an energy of lattice vibrations U at varying temperature T:

$$U(T) = 9Nk_BT(T/\theta_D)^3 \int_0^{\theta_D/T} \frac{x^3}{e^x-1}dx \quad (4)$$

for a sample with N atoms where x is unitless and U is in J (Kittel 2005). Various parameterizations may approximately relate this quantity to the volume, with one simple relation for low-temperature data being:

$$V = V_{0,0K} + U(\gamma_{th}/K_{0,0K}) \quad (5)$$

where $V_{0,0K}$ and $K_{0,0K}$ are the volume and isothermal bulk modulus at 1 bar and 0 K, respectively, while γ_{th} is the thermodynamic Grüneisen parameter at 1 bar (Wallace 1998; Knight and Price 2008; Meusburger et al. 2023). Equation 5 holds for V and $V_{0,0K}$ with units of m^3 and $K_{0,0K}$ with units of Pa, whereas V, $V_{0,0K}$, and $K_{0,0K}$ will be reported throughout this study in terms of Å^3, Å^3, and GPa, respectively. γ_{th} is dimensionless. Note that the relation in Equation 5 assumes temperature invariance in γ_{th} (Wallace 1998).

Experimental Methods

Römerite hand samples were obtained from CIT-15681, a rock sample in the Caltech Mineral Collection containing römerite alongside a halotrichite-group mineral, likely halotrichite or bilinite, and a black mineral, likely voltaite. These accessory minerals were identified based on their visual appearance (crystal habit and color) and known association with römerite. All are hydrated sulfates with Fe^{2+} and/or Fe^{3+}, with halotrichite and voltaite additionally hosting Al and (Al,K), respectively (Palmer et al. 2011; Majzlan et al. 2013). Hand samples of römerite were cleaned with ethanol, then lightly rolled and crushed to isolate single crystals, with viable crystals identified under cross-polarized light. Single crystals were analyzed on a Renishaw inVia microRaman Spectrometer System with a spectral resolution of 0.3 cm^{-1}, in part to confirm the consistency of the sample with römerite's spectrum. Raman spectroscopy was performed both prior to and following cleaning, confirming that the samples were not chemically altered by cleaning. We performed measurements with a 514.5 nm, 100 mW laser, with a 10 s collection time, repeated over 10 accumulations. Prior to measurements, the instrument was calibrated using a silicon standard. The spectrum from a single location on one crystal is plotted in Figure 2.

One of these single crystals was further analyzed with synchrotron time-domain Mössbauer spectroscopy (SMS), which eliminates source-broadening effects in the measured spectra, compared with energy-domain Mössbauer spectroscopy (e.g., Sturhahn 2004). In this analysis, the single crystal, 50 µm thick, was placed on a plexiglass glass slide for measurement. One ambient condition SMS measurement was performed at sector 3-ID-B at the Advanced Photon Source at Argonne National Laboratory. The measurement was conducted operating in 24-bunch mode. A tunable, high-resolution monochromator was used to tune monochromatic X–rays to the nuclear resonance energy of ^{57}Fe (14.4125 keV) with an energy spectrum full-width half maximum of 1 meV (Toellner 2000). Time spectra were collected between delay times of 25–135 ns after excitation via a downstream avalanche photo diode (APD) placed in the beam path and conventional time-filtering electronics. Signal from the römerite grain was optimized to 1–2 Hz, which is a typical signal strength for samples of this composition with natural ^{57}Fe abundance (Ratschbacher et al. 2023). Total collection time was 5 h and 47 min.

X-ray diffraction was performed on one of the single crystals of römerite samples, using a Bruker AXS D8 VENTURE four-circle diffractometer, equipped with a molybdenum microbeam source of wavelength 0.71073 Å. Prior to a full run of X-ray diffraction measurements, a final sample screening was performed on the diffractometer to select a viable single crystal without twinning and with high-intensity reflections to minimize collection time. X-ray diffraction measurements were taken as the sample was cooled to 100 K and as it was heated from 100 to 300 K. In both cases, the sample was measured at 5 K intervals between 260 and 300 K, and at 20 K intervals between 100 and 260 K. Data collection was performed over the course of ~3 h at each temperature step. Samples were cooled using a stream of liquid nitrogen from an Oxford Cryosystems Cryostream 700.

Downloaded from http://pubs.geoscienceworld.org/msa/ammin/article-pdf/110/6/933/7212453/ammin-2024-9432.1.pdf
by California Institute of Technology , Elijah Bird

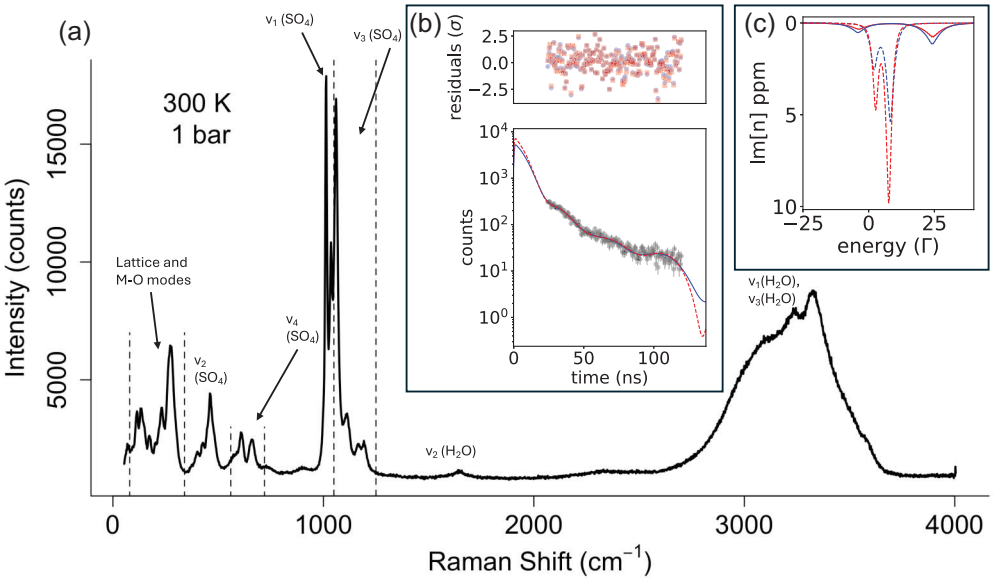

Figure 2. (**a**) Raman spectrum of römerite sample. (**b**) Fit to SMS data with a Lamb-Mössbauer factors of 0.6 and 0.8. The *y*-axis of the plots is in counts following 5 h and 47 min of collection. The fit with a Lamb-Mössbauer factor of 0.6 is plotted as a solid blue line, while the fit with a Lamb-Mössbauer factor of 0.8 is plotted as a dashed red line. The residuals are plotted as blue circles and red squares, respectively, in the panel's upper plot. (**c**) Forward modeled energy spectra for each fit to the time spectrum. The fit with a Lamb-Mössbauer factor of 0.6 is plotted in blue, while the fit with a Lamb-Mössbauer factor of 0.8 is plotted in red. Site 1 (Fe^{2+}) spectra are shown as solid lines and site 2 (Fe^{3+}) spectra are shown as dashed lines.

Bruker APEX3 software was utilized in harvesting and indexing reflections from the raw diffractometer output, determining lattice parameters, and reducing data. The unit-cell structure was solved and refined in the Olex 2 GUI using SHELX software. In general, we allowed atomic locations to vary during this processing, but restrained the interatomic distances of hydrogen atoms whose positions are not well constrained by these experimental methods. Particularly, in each water group, we imposed a length close to 0.82 Å for each O-H bond. Furthermore, we required that all water groups observed similar interatomic distances between hydrogen atoms.

Data

An example Raman spectrum and the collected Mössbauer spectrum are presented in Figure 2. Peaks in the Raman spectrum are reasonably consistent with those observed in Mauro et al. (2019), with modes generally appearing at the wavenumbers observed in said study. A broad hump associated with symmetric and antisymmetric vibrational modes of H_2O—$\nu_1(H_2O)$ and $\nu_3(H_2O)$, respectively—is observed between 2700 and 3600 cm^{-1}. Given the presence of 14 symmetrically independent water groups whose modes overlap at room temperature, we do not claim to resolve individual modes within the hump. The observed space group ($P\bar{1}$) is consistent with those reported in Fanfani et al. (1970), and the ambient-condition unit-cell parameters are in reasonable agreement, although *a*, *c*, and α are reduced by 0.01 Å, 0.03 Å, and 0.3°, respectively (the remaining parameters agree within uncertainty). The ambient-condition parameters are also in excellent agreement with those of synthetic römerite, with all lattice lengths agreeing within 0.004 Å and all lattice angles agreeing within 0.03° (Mereiter 2018). While no chemical composition was measured, this agreement suggests that the studied römerite sample is reasonably pure.

Lattice parameters (Fig. 3), atom locations, densities, and unit-cell volumes (Figs. 3–5; Online Materials[1] Fig. S1) were derived from single-crystal X-ray diffraction as a function of temperature. The unit-cell volume appears to increase continuously with increasing temperature, ranging from 603.6 to 610.8 Å^3, where the uncertainties are shown in Figure 5. The same is true for unit-cell parameters *a* and *b*, which increase from 6.395 to 6.450 Å and from 15.196 to 15.315 Å, respectively, as temperature increases from 100 to 300 K. In contrast, lattice parameter *c* contracts from 6.338 to 6.316 Å as temperature increases. Unit-cell angles α and β do not behave monotonically over the measured temperature range, with both parameters taking on minimum values (of 89.64° and 100.71°, respectively) at 120 K. Both angles increase for the remainder of the temperature series, taking on respective maxima of 90.20° and 100.95° at 300 K. Finally, lattice angle γ decreases from a maximum of 86.02° at 100 K to a minimum of 85.84° at 300 K. Atom locations at ambient conditions and complete volume and lattice parameter measurements are listed in Online Materials[1] Tables S1–S2.

The value of V/V_{300K}, the unitless ratio of the unit-cell volume to the volume at a reference temperature of 300 K, decreases more dramatically for römerite than for denser hydrous sulfates, kieserite ($MgSO_4{\cdot}H_2O$) and szomolnokite ($Fe^{2+}SO_4{\cdot}H_2O$) (Talla and Wildner 2019). Relative to blödite {$[Na_2Mg(SO_4)_2]{\cdot}4H_2O$}, a hydrous sulfate of similar density (Comodi et al. 2017), the value of V/V_{300K} for römerite decreases more rapidly from 300 to 200 K but sees a less intense decline between 200 and 100 K (Online Materials[1] Fig. S1). The measured ambient condition lattice parameters and volume are placed in the context of other hydrous sulfates in Table 1.

Analysis

We fit the SMS data with two values of the Lamb-Mössbauer factor [0.6 and 0.8, approximately corresponding to ferrous and ferric iron in sulfates, respectively (Dauphas et al. 2012; Pardo et al. 2023)], and with two sites. The thickness, texture, and site weights were allowed to vary, along with the quadrupole splitting and FWHM of both sites and the isomer shift of site 1. In both fits, the isomer shift of site 2 is set to 0.5. Fitting was performed in the CONUSS software package (Sturhahn 2000).

Volume data (unit-cell volume, a^3, b^3, and c^3) are fit to three parameterizations of the thermal expansion:

(1) The empirical model described by Equations 2 and 3, as discussed in Fei (Fei 1995): "Fei (1995)."

(2) A simplified version of the empirical model (Fei 1995), where Equation 2 is truncated to $\alpha(T) = a_0 + a_1 T$: "Fei (1995), linear."

(3) The physical Debye model described by Equations 4 and 5: "Debye model."

The choice to fit the cubes of the lattice cell lengths, rather than the lengths themselves, is in line with past work on the subject (e.g., Meusburger et al. 2023). Both empirical models may be fit with a least-squares approach, while the Debye model is fit using Newton's Method (Kincaid and Cheney 2009).

We constrain uncertainty in each model using Monte Carlo simulations. The *i*th temperature sampled of *n* total samples, T_i has an associated distribution of possible volumes $\mathbf{V_i}$. $\mathbf{V_i}$, for example, may be characterized by a normal distribution with mean and standard deviation equal to the observed volume and volume uncertainty at T_i. That is:

$$V_i = \mathcal{N}(V_i^{\text{obs}}, dV_i^{\text{obs}}) \quad (6)$$

During the *j*th Monte Carlo simulation, the volume at temperature T_i, V_{ij}, is randomly selected from $\mathbf{V_i}$. Taking T_i and V_{ij} for $i = 1, 2, \ldots, n$ as the temperature

Downloaded from http://pubs.geoscienceworld.org/msa/ammin/article-pdf/110/6/933/7212453/ammin-2024-9432.1.pdf
by California Institute of Technology . Elijah Bird

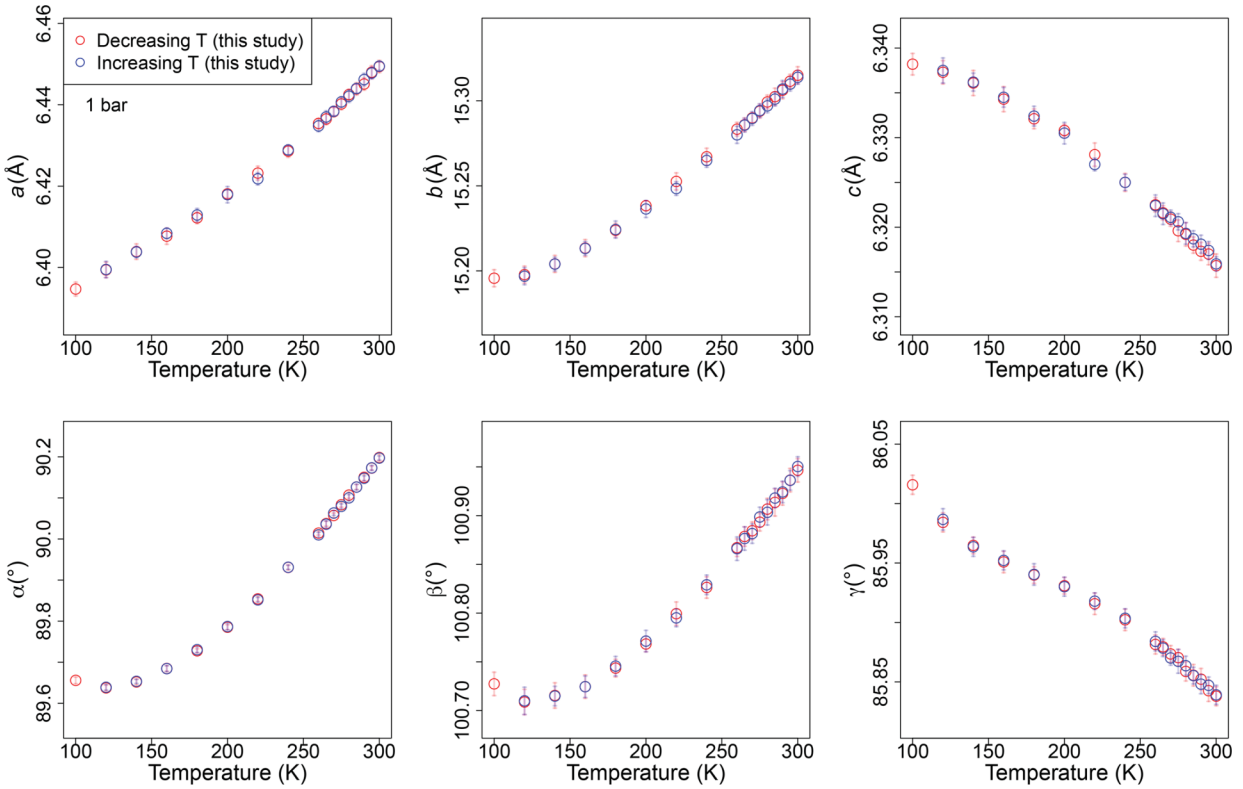

Figure 3. Lattice parameters *a*, *b*, *c*, α, β, and γ at varying temperatures at 1 bar.

and volume data for simulation *j*, we may invert for a model of the thermal expansion coefficient associated with the simulation, $\alpha_j(T)$. After performing *m* simulations, the uncertainty in the thermal expansion coefficient at T_i may be characterized by typical measures of data spread. For example, the standard deviation:

$$\sigma_{\alpha_{T_i}} = \sqrt{\frac{\sum_{j=1}^{n}\left[\alpha_j(T_i) - \frac{1}{n}\sum_{j=1}^{n}\alpha_j(T_i)\right]^2}{n}} \quad (7)$$

To better characterize the thermodynamic anisotropy of römerite, we calculate the eigenvalues of the Lagrangian infinitesimal thermal expansion tensor at varying temperature steps (ε_i), with reference to the ambient-temperature unit cell (Fig. 4; Online Materials[1] Table S3). The eigenvector corresponding to each eigenvalue is reported as its orientation relative to the crystal lattice axes ($\varepsilon_i \wedge a$, $\varepsilon_i \wedge b$, $\varepsilon_i \wedge c$, Online Materials[1] Table S3). These values are calculated with the software EoSFit7c using the decreasing temperature series from our experiment (Angel et al. 2014). The thermal expansion tensor remains strongly anisotropic across the temperature series, with an average anisotropy of (ε_1:ε_2:ε_3) = (1.0:1.51:−0.98). The relative magnitudes and orientations of the eigenvectors remain reasonably constant across the temperature series. We also calculate the negative thermal expansion eigenvalue and volume thermal expansion between temperatures 280 and 300 K, as this allows for more direct comparison with past discussions of negative thermal expansion in Meusburger et al. (2023).

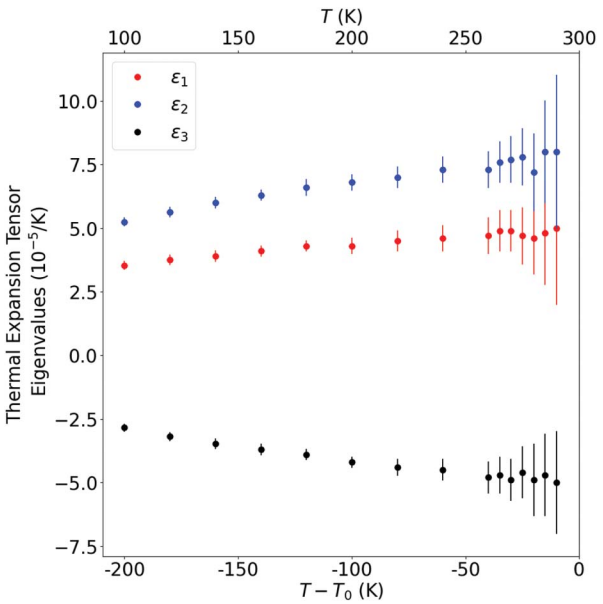

Figure 4. Eigenvalues of the Lagrangian infinitesimal thermal expansion tensor, with reference to $T_0 = 300$ K.

Results

Both SMS parameterizations (assuming respective Lamb-Mössbauer factors of 0.6 and 0.8) can fit the data excellently, with χ^2 values of less than 1.3 (1.21 and 1.27, respectively; Fig. 2). The best fits are reported in Table 2. The error correlation matrices associated with each of these parameterizations are reported in Online Materials[1] Table S4.

Each of the three models of thermal expansion is capable of fitting the data within error (see Fig. 5), and one's choice of model is dependent on the desired model properties. After setting the a_2 term to zero, the empirical model is the simplest of the parameterizations, requiring a linear fit of two terms. In contrast, the Debye model is more complex, requiring a nonlinear fit of

Downloaded from http://pubs.geoscienceworld.org/msa/ammin/article-pdf/110/6/933/7212453/ammin-2024-9432.1.pdf
by California Institute of Technology . Elijah Bird

Table 1. Ambient-condition lattice parameters and volumes of hydrous sulfates

	Römerite (this study)	Römerite (Fanfani et al. 1970)	Synthetic römerite (Mereiter 2018)
a (Å)	6.4494(15)	6.463(8)	6.4521(4)
b (Å)	15.315(5)	15.309(18)	15.3158(19)
c (Å)	6.3157(13)	6.341(8)	6.3190(4)
α (°)	90.1983(80)	90.53(17)	90.172(3)
β (°)	100.947(12)	101.08(17)	100.935(3)
γ (°)	85.8380(80)	85.73(17)	85.855(3)
V (Å^3)	610.82(47)	614.0(2.3)	611.45
Space Group	$P\bar{1}$	$P\bar{1}$	$P\bar{1}$

	Kieserite (Talla and Wildner 2019)	Szomolnokite (Talla and Wildner 2019)	Halotrichite (Zhitova et al. 2023)	Blödite (Comodi et al. 2014)
a (Å)	6.910(1)	7.086(1)	6.1947(2)	11.115(9)
b (Å)	7.634(2)	7.555(1)	24.2966(8)	8.242(2)
c (Å)	7.643(2)	7.780(1)	21.0593(8)	5.538(1)
α (°)				
β (°)	118.00(1)	118.61(1)	96.512(4)	100.82(4)
γ (°)				
V (Å^3)	356.00(14)	365.63(8)	3149.2(2)	498.4(7)
Space Group	*C*2/*c*	*C*2/*c*	$P2_1/n$	$P2_1/a$

Table 2. Parameterization of best-fit models to the Mössbauer spectrum

	Model 1	Model 2
Lamb-Mössbauer Factor	0.6	0.8
Thickness (μm)	38(6)	41(4)
Texture (%)	76(10)	74(5)
χ^2	1.206	1.272
Site 1 (Fe^{2+})		
δ_1 (mm/s)	1.00(3)	0.98(2)
Δ_1 (mm/s)	2.73(5)	2.74(4)
weight 1	0.33(3)	0.29(2)
FWHM 1 (mm/s)	0.51(3)	0.42(3)
Site 2 (Fe^{3+})		
δ_2 (mm/s)	0.5	0.5
Δ_2 (mm/s)	0.60(3)	0.49(4)
weight 2	0.67(3)	0.71(2)
FWHM 2 (mm/s)	0.166(4)	0.113(4)

Note: The columns assume different values of the Lamb-Mössbauer Factor.

three variables, but it provides a physical characterization of thermal expansion. As the Debye model parameters have physical meaning, they present additional insights into the thermodynamic properties of römerite. Furthermore, the model's physicality allows for more realistic extrapolation to lower temperatures. This is a vital capability, as the lowest temperature sampled in X-ray diffraction was 100 K, and relevant planetary contexts may observe temperatures as low as 40 K.

The a_2 term in the empirical model discussed in Fei (1995) does not appear to improve the model fit meaningfully. Furthermore, the term ensures nonphysical behavior in low-temperature extrapolations, due to the singularity at 0 K in its parameterization of α. Expected values for Debye model parameters, $K_{0,0K}/\gamma_{th}$ (GPa), $V_{0,0K}$ (Å^3), and θ_D (K), are listed in Online Materials[1] Table S5.

For the unit-cell, the Debye temperature is 610 K with an uncertainty of 151 K, $V_{0,0K}$ is 603.2 Å^3 with an uncertainty of 0.5 Å^3, and $K_{0,0K}/\gamma_{th}$ is 46 GPa with an uncertainty of 8 GPa. The table includes model parameters derived for the temperature series of cubed unit-cell lengths, which, while less physically meaningful, can accurately fit the data.

Discussion

The results of SMS are in agreement with our understanding of römerite's chemistry. In contrast to Dyar et al. (2013), where several natural römerite samples were analyzed and between three and five sites were used to fit the data, we were able to fit the spectrum with two iron sites. The quadrupole splitting and relative isomer shifts of the sites are consistent with high-spin ferrous iron and ferric iron, respectively (e.g., Dyar et al. 2006). The weight of site 2 is approximately twice that of site 1, consistent with a unit cell containing two ferric iron octahedra and one ferrous iron octahedron.

The reduction in lattice parameter *c* with increasing temperature is generally atypical but has a precedent in the szomolnokite-kieserite solid-solution series, for which thermal contraction is observed along the *b*-axis (Talla and Wildner 2019). Furthermore, various hydrous sulfates present thermal expansion tensors with one negative eigenvalue (Meusburger et al. 2023). We compare the anisotropy of thermal expansion with that of other hydrous sulfates in Online Materials[1] Table S6. Due to differing reference temperatures, direct comparison of negative thermal expansion is difficult, but the negative thermal expansion of römerite is as large as any of those listed and is four to five times larger than that of certain minerals (e.g., rozenite, meridianiite).

This effect appears to be tied to polyhedral rotations, similar to those observed in Wildner et al. (2022). The rotation of polyhedra can allow for an overall increase in the volume with a decrease along a particular lattice axis (in the case of römerite, the *c*-axis), resulting in a strong anisotropy of thermal expansion. The relative rotations of the polyhedra are evidenced by an increase in angles S3-O8-Fe1 and S4-O1-Fe1 (Online Materials[1] Fig. S2), both of which bridge the Fe^{3+}-centered octahedron with adjacent tetrahedra. One could demonstrate a physical mechanism for this thermal contraction through future measurements of the low-temperature vibrational and electronic dynamics of römerite, using techniques such as infrared spectroscopy (Pardo 2023) or SMS, respectively.

Our fit to the Debye model can broadly aid understanding of the physical properties of römerite. For unit-cell volume, $V_{0,0K}$ is the parameter most tightly constrained by the Debye model, with a standard error of 0.5 Å^3 (<0.1% of the unit-cell volume), while the remaining parameters are generally only constrained to a single significant digit. Modeled values of $K_{0,0K}/\gamma_{th}$ are negatively correlated with those of θ_D and $V_{0,0K}$, while θ_D and $V_{0,0K}$ are positively correlated (Table 3; Online Materials[1] Fig. S3).

Downloaded from http://pubs.geoscienceworld.org/msa/ammin/article-pdf/110/6/933/7212453/ammin-2024-9432.1.pdf
by California Institute of Technology , Elijah Bird

Table 3. Correlation matrix of Debye Model parameters for the thermal expansion of römerite's unit cell

	θ_D	$V_{0,0K}$	$K_{0,0K}/\gamma_{th}$
θ_D	1.00	0.94	−0.98
$V_{0,0K}$	0.94	1.00	−0.87
$K_{0,0K}/\gamma_{th}$	−0.98	−0.87	1.00

$K_{0,0K}/\gamma_{th}$ has an expected value of 46 GPa, with an uncertainty of 8 GPa. The temperature dependence of the Grüneisen parameter may be approximated by the Mie-Grüneisen model:

$$\gamma_{th} = \gamma_{0,300K}(V/V_{0,300K})^q \quad (8)$$

Pardo et al. (2023) note that the values of $\gamma_{0,300K}$ and q are not well characterized for sulfates, but appear to take on respective ranges of 0.67–2.5 and 1.5–2.5. If the Grüneisen parameter of römerite is also fit by constants in these ranges, the possible values of $K_{0,0K}$ would have a lower bound at 25 GPa. While values of the bulk modulus at zero temperature and pressure are poorly constrained for hydrous sulfates, this lower bound is consistent with measured bulk moduli for hydrous sulfates at ambient pressure and temperature, with szomolnokite, epsomite, mirabilite, and blödite all taking on values between 19 and 46 GPa (Fortes et al. 2013; Gromnitskaya et al. 2013; Comodi et al. 2014; Pardo et al. 2023). We expect temperature dependence in the quantity, so these values should not necessarily be directly compared with our estimate of $K_{0,0K}$.

Our estimate of the Debye temperature allows for a very rough constraint on römerite's heat capacity at constant volume, C_V ($J{\cdot}K^{-1}$), which can be approximated at low temperatures through:

$$C_V \approx 234 N k_B \left(\frac{T}{\theta_D}\right)^3 \quad (9)$$

as discussed in Kittel (2005). As we cube the already poorly constrained θ_D, this estimate has little practical application in isolation.

Implications

Further experimental work would aid the use of römerite as an end-member in models of planetary bodies. Low-temperature specific heat measurements could allow for a more direct constraint on θ_D through Equation 9. Due to the substantial tradeoffs between the Debye model parameters reported in this work, a more tightly constrained value of θ_D would also improve estimates of $V_{0,0K}$ and $K_{0,0K}/\gamma_{th}$. This work also highlights the value of the Debye model over empirical estimates on the thermal expansion coefficient in realistically extrapolating to behavior at low temperatures.

Low-temperature infrared spectroscopy, SMS, or nuclear resonant inelastic X-ray scattering (NRIXS) could likewise be highly informative. The former would allow for a clearer realization of the vibrational dynamics of römerite, which could clarify the physics of its anisotropic thermal expansion. NRIXS would aid in describing the seismic velocities of the mineral and Fe-specific vibrational quantities and force constants, as in Pardo et al. (2023), other valuable quantities for use in planetary studies.

Our description of the thermal expansion coefficient and other thermodynamic constants is of particular relevance to the behavior of Mars and the icy satellites, where hydrous sulfates are prevalent. While past studies have characterized the thermal behavior of other hydrous sulfates, römerite is a distinctive end-member composition, given its mixed-valence iron and high proportion of water, and its characterization aids our understanding of the full spectrum of hydrous sulfate behavior.

There remains ambiguity as to whether inferred hydrous sulfates on the icy satellites are of endogenic or exogenic origin. Considering the geographic character of spectral peaks on Europa, the radiolysis of endogenic rock by sulfur plasma from Io has been proposed as the source of the body's sulfur (Trumbo et al. 2020). Regardless, the dynamics of Europa's ice shell are poorly constrained at this time and may accommodate overturn (Buffo et al. 2020). This would provide a mechanism for material transport between the surface and ocean, in which case hydrous sulfates could more broadly pervade the body. Interactions with Io's plasma torus could also produce complex oxidation states on the surface of the jovian moons, such that mixed-valence minerals like römerite may be relevant. Therefore, the study of mixed-valence hydrous sulfates is of general interest, as the specimens may only be produced under distinct redox conditions. Through laboratory experiments, one may characterize the stability fields of various sulfates (Chou et al. 2013). Results like those reported in our study may aid in bridging from an understanding of a planetary body's redox environment to the characterization of its thermodynamics, or vice versa.

While hydrous sulfates are particularly prevalent on the martian and europan surfaces, they are potentially relevant to myriad planetary bodies. Any quantity of hydrous sulfates on Earth's moon could provide insights into the history of lunar water, for example. This is an area of continued interest, as studies have demonstrated the presence of hydrous materials on the lunar surface, but the hydration of the bulk moon and the history of water on the body are poorly constrained (Saal et al. 2008; McCubbin et al. 2010; Honniball et al. 2021). Given that most solar system bodies observe lower temperatures than Earth (e.g., the equator of Earth's moon reaches temperatures as low as 100 K), an understanding of the behavior of hydrous sulfates under low temperature is critical (Malla and Brown 2015). For example, hydrous sulfates that observe negative thermal expansion along an eigenvector, such as römerite, could cause sulfate-rich aggregates in low-temperature environments to take on preferred orientations as they deform.

As the low-temperature measurements in this study were performed at ambient pressure, our results primarily provide constraints on the behavior of hydrous sulfates at shallow depths within planetary bodies. Alongside the results of this study, X-ray diffraction measurements of römerite at low temperatures under compression would provide meaningful constraints on the mineral's equation of state. For a reasonable choice of sampled pressures, such measurements could better characterize the behavior of the end-member hydrous sulfate in models of the interiors of icy satellites.

Acknowledgments and Funding

We thank Michael K. Takase and the Caltech X-ray Diffraction Facility (XRCF) for operation of the diffractometer. The XRCF is supported by the Dow Next Generation Instrumentation Grant and the Beckman Institute. We thank

Downloaded from http://pubs.geoscienceworld.org/msa/ammin/article-pdf/110/6/933/7212453/ammin-2024-9432.1.pdf
by California Institute of Technology , Elijah Bird

George Rossman for assistance in sample collection and for use of his laboratory in Raman spectroscopy measurements. We appreciate helpful discussions with Wolfgang Sturhahn, Benjamin Strozewski, and Cijin Zhou. We thank Ross Angel for valuable insights into his EoSFit7 software. We thank G. Diego Gatta, the associate editor assigned to our manuscript. Likewise, we appreciate the insightful reviews provided by Johannes Meusburger, Azzurra Zucchini, and an anonymous reviewer. We thank NSF-CSEDI (EAR-2009935, -2303148) for supporting this work. This research used resources of the Advanced Photon Source, a U.S. Department of Energy (DOE) Office of Science User Facility operated for the DOE Office of Science by Argonne National Laboratory under Contract No. DE-AC02-06CH11357. Beamline 3-ID-B at the Advanced Photon Source was partially supported by COMPRES, the Consortium for Materials Properties Research in Earth Sciences under NSF cooperative agreement EAR-1606856.

References Cited

Angel, R.J., Alvaro, M., and Gonzalez-Platas, J. (2014) EosFit7c and a Fortran module (library) for equation of state calculations. Zeitschrift für Kristallographie - Crystalline Materials, 229, 405–419, https://doi.org/10.1515/zkri-2013-1711.

Ashkenazy, Y. (2019) The surface temperature of Europa. Heliyon, 5, e01908, https://doi.org/10.1016/j.heliyon.2019.e01908.

Bishop, J.L., Parente, M., Weitz, C.M., Noe Dobrea, E.Z., Roach, L.H., Murchie, S.L., McGuire, P.C., McKeown, N.K., Rossi, C.M., Brown, A.J., and others. (2009) Mineralogy of Juventae Chasma: Sulfates in the light-toned mounds, mafic minerals in the bedrock, and hydrated silica and hydroxylated ferric sulfate on the plateau. Journal of Geophysical Research. Planets, 114, E00D09.

Buffo, J.J., Schmidt, B.E., Huber, C., and Walker, C.C. (2020) Entrainment and dynamics of ocean-derived impurities within Europa's ice shell. Journal of Geophysical Research: Planets, 125, e2020JE006394.

Chou, I.-M., Seal, R.R. II, and Wang, A. (2013) The stability of sulfate and hydrated sulfate minerals near ambient conditions and their significance in environmental and planetary sciences. Journal of Asian Earth Sciences, 62, 734–758, https://doi.org/10.1016/j.jseaes.2012.11.027.

Comodi, P., Nazzareni, S., Balić-Žunić, T., Zucchini, A., and Hanfland, M. (2014) The high-pressure behavior of bloedite: A synchrotron single-crystal X-ray diffraction study. American Mineralogist, 99, 511–518, https://doi.org/10.2138/am.2014.4640.

Comodi, P., Stagno, V., Zucchini, A., Fei, Y., and Prakapenka, V. (2017) The compression behavior of blödite at low and high temperature up to ~10 GPa: Implications for the stability of hydrous sulfates on icy planetary bodies. Icarus, 285, 137–144, https://doi.org/10.1016/j.icarus.2016.11.032.

Dalton, J.B. III, Shirley, J.H., and Kamp, L.W. (2012) Europa's icy bright plains and dark linea: Exogenic and endogenic contributions to composition and surface properties. Journal of Geophysical Research: Planets, 117, E03003.

Dauphas, N., Roskosz, M., Alp, E.E., Golden, D.C., Sio, C.K., Tissot, F.L.H., Hu, M.Y., Zhao, J., Gao, L., and Morris, R.V. (2012) A general moment NRIXS approach to the determination of equilibrium Fe isotopic fractionation factors: Application to goethite and jarosite. Geochimica et Cosmochimica Acta, 94, 254–275, https://doi.org/10.1016/j.gca.2012.06.013.

Dyar, M.D., Agresti, D.G., Schaefer, M.W., Grant, C.A., and Sklute, E.C. (2006) Mössbauer spectroscopy of Earth and planetary materials. Annual Review of Earth and Planetary Sciences, 34, 83–125, https://doi.org/10.1146/annurev.earth.34.031405.125049.

Dyar, M.D., Breves, E., Jawin, E., Marchand, G., Nelms, M., O'Connor, V., Peel, S., Rothstein, Y., Sklute, E.C., Lane, M.D., and others. (2013) Mössbauer parameters of iron in sulfate minerals. American Mineralogist, 98, 1943–1965, https://doi.org/10.2138/am.2013.4604.

Fanfani, L., Nunzi, A., and Zanazzi, P.F. (1970) The crystal structure of roemerite. American Mineralogist. Journal of Earth and Planetary Materials, 55, 78–89.

Fei, Y. (1995) Thermal expansion. In T.J. Ahrens, Ed., Mineral Physics & Crystallography, pp. 29–44. American Geophysical Union (AGU).

Fortes, A.D., Wood, I.G., Alfredsson, M., Vočadlo, L., and Knight, K.S. (2006) The thermoelastic properties of $MgSO_4{\cdot}7D_2O$ (epsomite) from powder neutron diffraction and *ab initio* calculation. European Journal of Mineralogy, 18, 449–462, https://doi.org/10.1127/0935-1221/2006/0018-0449.

Fortes, A.D., Wood, I.G., and Knight, K.S. (2008) The crystal structure and thermal expansion tensor of $MgSO_4{\cdot}11D_2O$ (meridianiite) determined by neutron powder diffraction. Physics and Chemistry of Minerals, 35, 207–221, https://doi.org/10.1007/s00269-008-0214-x.

Fortes, A.D., Brand, H.E.A., Vočadlo, L., Lindsay-Scott, A., Fernandez-Alonso, F., and Wood, I.G. (2013) *P-V-T* equation of state of synthetic mirabilite ($Na_2SO_4{\cdot}10D_2O$) determined by powder neutron diffraction. Journal of Applied Crystallography, 46, 448–460, https://doi.org/10.1107/S0021889813001362.

Gromnitskaya, E.L., Yagafarov, O.F., Lyapin, A.G., Brazhkin, V.V., Wood, I.G., Tucker, M.G., and Fortes, A.D. (2013) The high-pressure phase diagram of synthetic epsomite ($MgSO_4{\cdot}7H_2O$ and $MgSO_4{\cdot}7D_2O$) from ultrasonic and neutron powder diffraction measurements. Physics and Chemistry of Minerals, 40, 271–285, https://doi.org/10.1007/s00269-013-0567-7.

Honniball, C.I., Lucey, P.G., Li, S., Shenoy, S., Orlando, T.M., Hibbitts, C.A., Hurley, D.M., and Farrell, W.M. (2021) Molecular water detected on the sunlit Moon by SOFIA. Nature Astronomy, 5, 121–127, https://doi.org/10.1038/s41550-020-01222-x.

Kincaid, D.R. and Cheney, E.W. (2009) Numerical Analysis: Mathematics of scientific computing, Volume 2, 788 p. American Mathematical Society.

Kittel, C. (2005) Introduction to Solid State Physics, 704 p. Wiley.

Knight, K.S. and Price, G.D. (2008) Powder neutron-diffraction studies of clinopyroxenes. I. The crystal structure and thermoelastic properties of jadeite between 1.5 and 270 K. Canadian Mineralogist, 46, 1593–1622, https://doi.org/10.3749/canmin.46.6.1593.

Lichtenberg, K.A., Arvidson, R.E., Morris, R.V., Murchie, S.L., Bishop, J.L., Fernandez Remolar, D., Glotch, T.D., Noe Dobrea, E., Mustard, J.F., Andrews-Hanna, J., and others. (2010) Stratigraphy of hydrated sulfates in the sedimentary deposits of Aram Chaos, Mars. Journal of Geophysical Research: Planets, 115, E00D17.

Majzlan, J., Schlicht, H., Wierzbicka-Wieczorek, M., Giester, G., Pöllmann, H., Brömme, B., Doyle, S., Buth, G., and Bender Koch, C. (2013) A contribution to the crystal chemistry of the voltaite group: Solid solutions, Mössbauer and infrared spectra, and anomalous anisotropy. Mineralogy and Petrology, 107, 221–233, https://doi.org/10.1007/s00710-012-0254-2.

Malla, R.B. and Brown, K.M. (2015) Determination of temperature variation on lunar surface and subsurface for habitat analysis and design. Acta Astronautica, 107, 196–207, https://doi.org/10.1016/j.actaastro.2014.10.038.

Martínez, G.M., Newman, C.N., De Vicente-Retortillo, A., Fischer, E., Renno, N.O., Richardson, M.I., Fairén, A.G., Genzer, M., Guzewich, S.D., Haberle, R.M., and others. (2017) The modern near-surface martian climate: A review of in-situ meteorological data from Viking to Curiosity. Space Science Reviews, 212, 295–338, https://doi.org/10.1007/s11214-017-0360-x.

Mauro, D., Biagioni, C., Pasero, M., and Zaccarini, F. (2019) Crystal-chemistry of sulfates from Apuan Alps (Tuscany, Italy). II. Crystal structure and hydrogen bonding system of römerite, $Fe^{2+}Fe^{3+}_2(SO_4)_4(H_2O)_{14}$. Atti della Societa Toscana di Scienze Naturali, 125, 5–11.

McCubbin, F.M., Steele, A., Hauri, E.H., Nekvasil, H., Yamashita, S., and Hemley, R.J. (2010) Nominally hydrous magmatism on the Moon. Proceedings of the National Academy of Sciences of the United States of America, 107, 11223–11228, https://doi.org/10.1073/pnas.1006677107.

Mereiter, K. (2018) Experimental Crystal Structure Determination. Cambridge Crystallographic Data Centre.

Meusburger, J.M., Hudson-Edwards, K.A., Tang, C.C., Connolly, E.T., Crane, R.A., and Fortes, A.D. (2023) Low-temperature crystallography and vibrational properties of rozenite ($FeSO_4{\cdot}4H_2O$), a candidate mineral component of the polyhydrated sulfate deposits on Mars. American Mineralogist, 108, 1080–1091, https://doi.org/10.2138/am-2022-8502.

Murchie, S.L., Mustard, J.F., Ehlmann, B.L., Milliken, R.E., Bishop, J.L., McKeown, N.K., Noe Dobrea, E.Z., Seelos, F.P., Buczkowski, D.L., Wiseman, S.M., and others. (2009) A synthesis of martian aqueous mineralogy after 1 Mars year of observations from the Mars Reconnaissance Orbiter. Journal of Geophysical Research. Planets, 114, E00D06.

Palmer, S.J., Reddy, B.J., and Frost, R.L. (2011) Synthesis and vibrational spectroscopy of halotrichite and bilinite. Spectrochimica Acta Part A: Molecular and Biomolecular Spectroscopy, 79, 69–73, https://doi.org/10.1016/j.saa.2011.02.001.

Pardo, O.S. (2023) The elastic, electronic, and structural properties of hydrous, sulfur-bearing minerals in planetary environments: From the surface to deep interiors, 161 p. Ph.D. thesis, California Institute of Technology.

Pardo, O.S., Dobrosavljevic, V.V., Sturhahn, W., Toellner, T.S., Strozewski, B., and Jackson, J.M. (2023) Lattice dynamics, sound velocities, and atomic environments of szomolnokite at high pressure. Physics and Chemistry of Minerals, 50, 32.

Ratschbacher, B.C., Jackson, J.M., Toellner, T.S., Bucholz, C.E., Sturhahn, W., and Solomatova, N.V. (2023) Fe^{3+}/Fe^{T} ratios of amphiboles determined by high spatial resolution single-crystal synchrotron Mössbauer spectroscopy. American Mineralogist, 108, 70–86, https://doi.org/10.2138/am-2022-8115.

Saal, A.E., Hauri, E.H., Cascio, M.L., Van Orman, J.A., Rutherford, M.C., and Cooper, R.F. (2008) Volatile content of lunar volcanic glasses and the presence of water in the Moon's interior. Nature, 454, 192–195, https://doi.org/10.1038/nature07047.

Shirley, J.H., Dalton, J.B. III, Prockter, L.M., and Kamp, L.W. (2010) Europa's ridged plains and smooth low albedo plains: Distinctive compositions and compositional gradients at the leading side-trailing side boundary. Icarus, 210, 358–384, https://doi.org/10.1016/j.icarus.2010.06.018.

Sturhahn, W. (2000) CONUSS and PHOENIX: Evaluation of nuclear resonant scattering data. Hyperfine Interactions, 125, 149–172, https://doi.org/10.1023/A:1012681503686.

——— (2004) Nuclear resonant spectroscopy. Journal of Physics: Condensed Matter, 16, S497–S530, https://doi.org/10.1088/0953-8984/16/5/009.

Talla, D. and Wildner, M. (2019) Investigation of the kieserite-szomolnokite solid-solution series, $(Mg,Fe)SO_4{\cdot}H_2O$, with relevance to Mars: Crystal chemistry, FTIR, and Raman spectroscopy under ambient and martian temperature conditions. American Mineralogist, 104, 1732–1749, https://doi.org/10.2138/am-2019-6983.

Downloaded from http://pubs.geoscienceworld.org/msa/ammin/article-pdf/110/6/933/7212453/ammin-2024-9432.1.pdf
by California Institute of Technology , Elijah Bird

Toellner, T.S. (2000) Monochromatization of synchrotron radiation for nuclear resonant scattering experiments. Hyperfine Interactions, 125, 3–28, https://doi.org/10.1023/A:1012621317798.

Trumbo, S.K., Brown, M.E., and Hand, K.P. (2020) Endogenic and exogenic contributions to visible-wavelength spectra of Europa's trailing hemisphere. The Astronomical Journal, 160, 282, https://doi.org/10.3847/1538-3881/abc34c.

Wallace, D.C. (1998) Thermodynamics of Crystals, 2nd ed., 512 p. Dover Publications.

Wildner, M., Zakharov, B.A., Bogdanov, N.E., Talla, D., Boldyreva, E.V., and Miletich, R. (2022) Crystallography relevant to Mars and Galilean icy moons: Crystal behavior of kieserite-type monohydrate sulfates at extraterrestrial conditions down to 15 K. IUCrJ, 9, 194–203, https://doi.org/10.1107/S2052252521012720.

Zhitova, E.S., Sheveleva, R.M., Zolotarev, A.A., Krivovichev, S.V., Shilovskikh, V.V., Nuzhdaev, A.A., and Nazarova, M.A. (2023) The crystal structure of magnesian halotrichite, $(Fe,Mg)Al_2(SO_4)_4{\cdot}22H_2O$: Hydrogen bonding, geometrical parameters and structural complexity. Journal of Geosciences, 68, 163–178, https://doi.org/10.3190/jgeosci.372.

Manuscript received April 19, 2024
Manuscript accepted October 23, 2024
Accepted manuscript online October 29, 2024
Manuscript Handled by G. Diego Gatta

Endnotes:

[1]Deposit item AM-25-69432. Online Materials are free to all readers. Go online, via the table of contents or article view, and find the tab or link for supplemental materials. The CIF has been peer-reviewed by our Technical Editors.

Downloaded from http://pubs.geoscienceworld.org/msa/ammin/article-pdf/110/6/933/7212453/ammin-2024-9432.1.pdf
by California Institute of Technology , Elijah Bird